2016

Shielded radiography with a laser-driven MeV-energy X-ray source

Shouyuan Chen
University of Nebraska–Lincoln, schen6@unl.edu

Grigory V. Golovin
University of Nebraska-Lincoln, ggolovin2@unl.edu

Cameron Miller
University of Michigan

Daniel Haden
University of Nebraska-Lincoln

Sudeep Banerjee
University of Nebraska–Lincoln, Sudeep.Banerjee@asu.edu

See next page for additional authors

Published in *Nuclear Instruments and Methods in Physics Research B* 366 (2016), pp. 217–223.
doi 10.1016/j.nimb.2015.11.007

Submitted 8 July 2015; revised 18 September 2015; accepted 3 November 2015; online 19 November 2015.

Shielded radiography with a laser-driven MeV-energy X-ray source

Shouyuan Chen,[1] Grigory Golovin,[1] Cameron Miller,[2] Daniel Haden,[1]
Sudeep Banerjee,[1] Ping Zhang,[1] Cheng Liu,[1] Jun Zhang,[1]
Baozhen Zhao,[1] Shaun Clarke,[2] Sara Pozzi,[2] and Donald Umstadter[1]

1 Department of Physics and Astronomy, University of Nebraska–Lincoln, Lincoln, NE 68588, USA
2 Department of Nuclear Engineering and Radiological Sciences, University of Michigan, Ann Arbor, MI 48109, USA

Corresponding author — D. Umstadter, email donald.umstadter@unl.edu

Abstract

We report the results of experimental and numerical-simulation studies of shielded radiography using narrowband MeV-energy X-rays from a compact all-laser-driven inverse-Compton-scattering X-ray light source. This recently developed X-ray light source is based on a laser-wakefield accelerator with ultra-high-field gradient (GeV/cm). We demonstrate experimentally high-quality radiographic imaging (image contrast of 0.4 and signal-to-noise ratio of 2:1) of a target composed of 8-mm thick depleted uranium shielded by 80-mm thick steel, using a 6-MeV X-ray beam with a spread of 45% (FWHM) and 107 photons in a single shot. The corresponding dose of the X-ray pulse measured in front of the target is ~100 nGy/pulse. Simulations performed using the Monte-Carlo code MCNPX accurately reproduce the experimental results. These simulations also demonstrate that the narrow bandwidth of the Compton X-ray source operating at 6 and 9 MeV leads to a reduction of deposited dose as compared to broadband bremsstrahlung sources with the same end-point energy. The X-ray beam's inherently low-divergence angle (~mrad) is advantageous and effective for interrogation at standoff distance. These results demonstrate significant benefits of all-laser driven Compton X-rays for shielded radiography.

Keywords: Radiography, Laser, Inverse Compton, Monte Carlo code

1. Introduction

Nuclear materials smuggling is considered to be a serious threat to global security [1]. Given the large number of cargo containers (over 100 million) that are transported around the world each year [2], they have long been considered as a possible vehicle for illegal transport of nuclear weapons and special nuclear materials (SNM). To mitigate this potential threat, it is critical to detect these illicit materials early, while they are in transport or upon their arrival at ports. Many detection technologies are currently in use at ports worldwide to detect SNM [3]. Passive technologies are a common method for SNM detection, and function by detecting radiation signatures emitted by SNM. However, certain SNM, such as highly enriched uranium, can be easily shielded to defeat passive detection [4].

Active interrogation technologies provide an alternative solution by detecting SNM based on other signatures of SNM materials, such as density and atomic number. Among the active interrogation technologies, including X-ray, neutron or muon radiography [5–7], X-ray radiography is the most mature technology for the detection of dense shielded materials. The requirements for safe and accurate inspection of cargo-containers are subject to multiple constraints, and this limits the choice of parameters for the X-ray beam. For instance, to achieve sufficient penetration through thick shielding, a photon energy of ~6 MeV is required [3,8]. Maintaining a safe level of radiological dosage to both the target and bystanders requires a relatively narrow X-ray bandwidth [9,10]. Material discrimination by means of the *Z*-scanning technique requires tunability of the X-ray photon energy. This technique exploits the fact that different materials have different energy dependence for the attenuation coefficient which enables them to be distinguished using dual or multi-energy radiography [11,12]. A highly collimated X-ray beam is required in a scenario where standoff interrogation is the only possibility [13]. Thus, there is currently significant effort worldwide to develop a single X-ray source that can simultaneously meet all of these stringent requirements.

The most commonly used X-ray source, based on bremsstrahlung radiation, produces the requisite energy, but it has a continuous energy spectrum and large divergence. Standard radioisotope sources produce narrow bandwidth X-rays [9], but their X-ray energies are restricted to 61.5 MeV and they cannot be tuned. Inverse-Compton-scattering (ICS) sources produce narrowband and tunable multi-MeV X-ray beams with a small angular spread and can simultaneously meet all of the requirements for shielded radiography. However, application of ICS sources based on conventional electron accelerators is limited by their large size [14,15]. The recently developed laser-wakefield-accel-

erator-driven inverse-Compton-scattering (LWFA-ICS) source overcomes all of these limitations by using a 1000 times higher acceleration gradient of a plasma wakefield compared with conventional RF technology, and provides a compact X-ray source with well-collimated (mrad), narrowband ($\Delta E/E \sim 0.5$), and tunable (from 1 to 9 MeV) beams [16–19].

In this paper, we experimentally demonstrate radiography of a shielded uranium target with a LWFA-ICS source [16–19]. Using numerical simulation and experimental results, we show that a LWFA-ICS source is an exciting new device for the radiography of cargo containers and can potentially have a transformative impact in this critical area.

2. Radiography with LWFA-ICS X-ray source

In the following, we report the results of the experiments that provide a proof-of-principle demonstration that low-dose, and high-contrast radiography can be performed with the LWFA-ICS X-ray source [16–18]. We first describe the characteristics of the source parameters that were used for this experiment followed by the results that were obtained for radiography of shielded depleted uranium targets as well as measurements of the X-ray dose. We then analyze the radiographic images to infer the image contrast and signal to noise ratio (SNR). MCNPX simulations are performed to predict the performance of the radiographic system and compared with experimental observations.

2.1. Electron and X-ray beam generation and characterization

The electron accelerator and the X-ray source are driven by the Diocles laser system housed in the Extreme Light Laboratory at the University of Nebraska-Lincoln. For this work, the laser was operated at a peak power of 150 TW. Fig. 1 shows the experimental setup used to generate high-energy X-rays as well as the layout for radiography experiments. The uncompressed 7-J laser beam was split using a 70% reflecting (30% transmitting) beam splitter. The reflected and transmitted beams were then directed into two independent grating pulse-compressors, and each was compressed to 35 fs, to be used as the drive and scattering beams, respectively. The drive laser pulse, with 3-J energy after the compressor, was focused by a 1-m off-axis parabola to a 20-μm (FWHM) focal spot, with 40% energy enclosed in the FWHM contour. The focus was located on the rising edge of a 6-mm-long supersonic gas target (99% helium and 1% nitrogen) at a height of 1.5 mm above the nozzle. The electron beam spectra were then measured with a magnetic spectrometer, consisting of a 5.5-in round magnet (0.7 T) and a 6-inch rectangular magnet (0.7 T) in series and detected on a fluorescent screen (LANEX) imaged by a 12-bit CCD camera. Due to the size limits of the LANEX, the spectrometer has an energy cutoff at 150 MeV.

Fig. 2(a) shows the typical spectrum measured for the electron beam. The electron beams had a charge of 50 pC, an angular divergence of ~5 mrad, and an energy spectrum that peaked at 500 MeV and extended to 600 MeV. The electron energy spectrum is obtained using the magnetic spectrometer and a deconvolution process is used to account for the angular divergence of the electron beam. Though LWFA accelerators with lower energy spread were demonstrated by separating the injection and acceleration stage [17], we chose a 6-mm single nozzle with ionization injection in this experiment. This accelerator was selected to provide the high charge and high energy electrons needed to generate ~6 MeV X-ray beams. The generated X-ray beam profile was first measured by a calibrated 50-mm by 50-mm voxelated CsI detector with 1-cm thickness coupled to a 14-bit EM gain camera positioned before the radiography target. The X-ray beam had a divergence of ~7 mrad and ~10^7 photons. Fig. 2(b) shows the calculated on-axis X-ray spectral intensity based on the electron spectrum, which is peaked at 6.5 MeV and extends up to 10 MeV with ~45% FWHM energy spread.

2.2. Radiography of shielded depleted uranium target

Subsequent to the characterization of the X-ray beam, we then used this MeV-energy beam for radiography. The radiography targets consisted of two layers of steel shielding (thicknesses varied from 6 mm to 40 mm) and uranium disks with 20-mm diameter and 6–8 mm thicknesses, as show in Fig. 3. The targets were positioned 3 m from the X-ray source. The radiography images were obtained by a 50-mm by 50-mm voxelated CsI with 2-cm thickness coupled to a 16-bit EMCCD camera operated in high-gain mode.

In what follows, we evaluate the quality of the radiography images using two parameters: the image contrast and signal to noise ratio (SNR). The absolute contrast is defined as the change in intensity caused by the structure of interest [20]. In other words, it is the change in intensity caused by the structure of interest compared with the surrounding material. A more useful definition is relative contrast C, which is defined as:

$$C = \frac{\Delta I}{I} \tag{1}$$

where I is the average background intensity (in the vicinity of the structure of interest), and DI is the change in the intensity caused by the structure of interest. The SNR is defined as

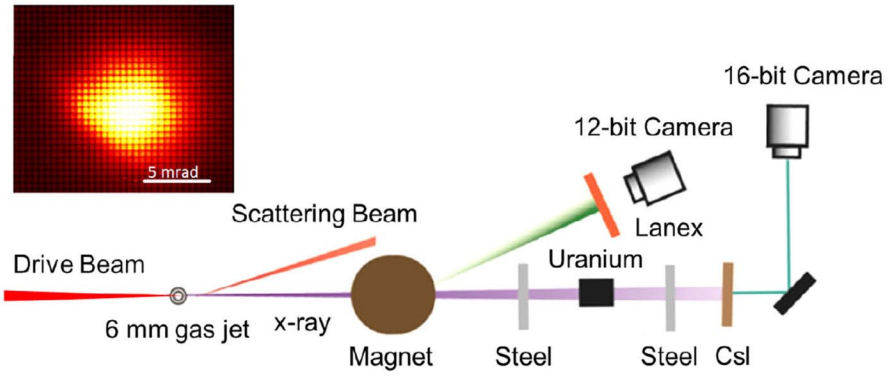

Fig. 1. Experimental setup for radiography experiment. The inset on the top-left shows the X-ray beam profile on the CsI detector. The angular divergence of the X-ray beam is 7 mrad (FWHM).

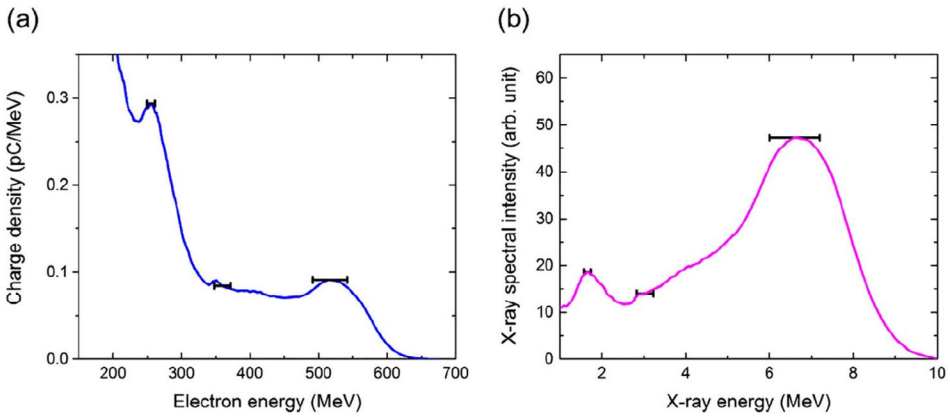

Fig. 2. Measured electron and X-ray energy spectra. (a) Electron energy spectrum with a high energy peak at 520 MeV and low energy tail. The error bars represent the standard deviation of the electron beam energy due to the electron beam pointing stability into the magnet spectrometer at three electron beam energies. (b) X-ray spectral intensity calculated based on the electron energy spectrum. The peaked X-ray spectrum is due to the fact that the spectral intensity is weighted by the X-ray energy. The error bars at the three X-ray energy points represent the uncertainty of X-ray energies at these points due to the error in the electron beam energy measurement.

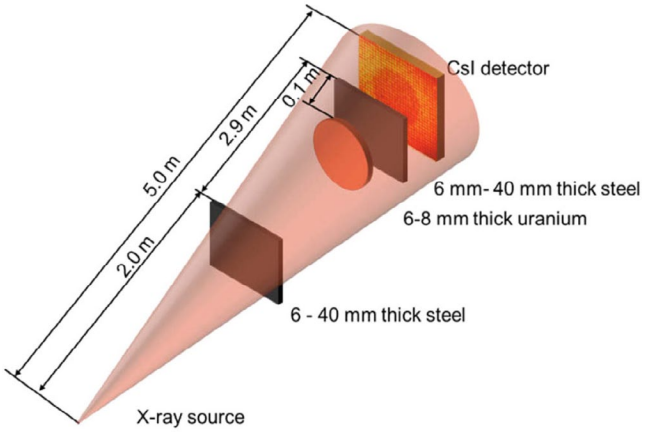

Fig. 3. Experimental setup used for radiography measurements. The high-energy X-ray beam is incident on a target composed of a depleted uranium disc shielded by steel plates. The transmitted X-ray beam is detected by a voxelated CsI detector.

$$\mathrm{SNR} = \frac{\Delta I}{\sigma_I} = C\frac{I}{\sigma_I} \tag{2}$$

where σ_I is the standard deviation of the background intensity.

In the experiment, we first took a radiograph image of a 6-mm thick uranium disk without shielding, as shown in Fig. 4(a). We analyzed the average intensity in two areas: the adjacent area of the background and the uranium disk covered by an area of 3 by 3 voxels, which have counts of ~9500 and ~4500, respectively. The standard deviation of the background intensity is ~900. Based on the contrast and SNR definition, the contrast of the image contrast is 0.46 and the SNR is ~4. We then took a radiograph of the 6-mm uranium disk shielded by 0.25-inch thick steel, both at the back and front, as shown in Fig. 4(b). Using the same procedure used for unshielded uranium, we analyzed the image SNR of the shielded uranium target with the image intensity in the uranium target area and the adjacent area. The intensity in the target area is 4250 counts and the adjacent area is 6480 counts. The standard deviation of the background intensity is about ~650 counts. The contrast of the image is ~0.39 and the SNR is ~3.

We then obtained radiographs of 8-mm uranium shielded by 1.5-inch steel in the front and back of the target. The radiography image is shown in Fig. 4(c). We performed the same image quality analysis and used the 3 by 3 voxel area in the target and adjacent area to obtain the contrast and SNR. The average intensity in the target area is 1750 counts and intensity in the adjacent area is 2960 counts with standard deviation of ~600 counts. This gives a contrast of ~0.41 and SNR of ~2. These images were also processed with a Fourier filter to suppress features associated with the grid on the CsI detector. As shown in Fig. 4(d)–(f), post-processing enhances the radiography image and makes it easier to distinguish the object.

The results indicate that the image contrast of the radiograph using the Thomson source was affected little by the increase in shielding thickness. The shielding mainly affected SNR since the signal level drops with more shielding. Even with total shielding of 3-inch steel, we were able to obtain an image with SNR of 2 using the current detection system with a single X-ray pulse. Using a more sensitive detection system, such as $CdWO_4$ coupled to a PMT sensor, and multiple shots, we believe the SNR would be further improved.

Another important parameter for cargo container scanning is the dosage of the X-ray beam. The X-ray dose was measured using an ion chamber dosimeter (Radcal model 10x6-1800), which has a sensitivity of 0.01 nGy. The measured single shot X-ray dose in front of the radiography target is ~100 nGy. This measurement is consistent with the calculated dose based on the X-ray energy spectrum and the photon number (10^7/pulse) measured by the calibrated CsI detector. Simulations discussed in a later section show that the narrowband X-ray beam can reduce the dose on the target by a factor of two. As a result, the narrowband X-ray source can better meet the dose requirements for X-rays used in cargo scanning: As Low as Reasonably Achievable (ALARA) [21].

The experimental results are compared with MCNPX simulation, using the same target geometry and X-ray spectrum shown in Fig. 5. The simulated image contrast is 0.40 for 0.25-inch steel shielded 6-mm thick uranium, and it is consistent with the experiment results of 0.39. For the case of 8-mm thick uranium shielded by 1.5-inch steel, the simulated image contrast is 0.42, which also reasonably agrees with the measured value of 0.41.

3. MCNPX simulation of narrowband X-ray radiography

Although the X-rays produced by LWFA-ICS sources have relatively low energy spreads ($\Delta E/E$ ~ 40%) compared to bremsstrahlung sources, their spreads are large compared with the gamma rays generated from naturally occurring radioactive isotopes. It is therefore reasonable to ask how the radiographic image con-

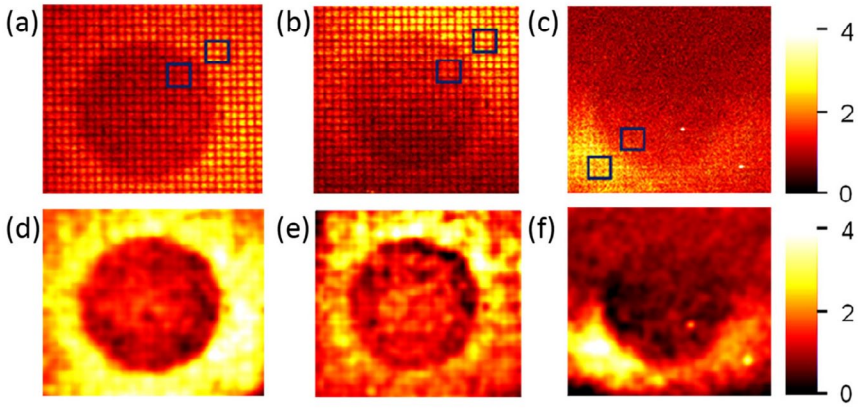

Fig. 4. Raw and processed radiography images of shielded uranium. (a) Radiography image of the 6-mm uranium disk without shielding. (b) Radiography image of the 6-mm uranium disk shielded by 0.25-in steel in back and front. (c) Radiography image of 8-mm uranium shielded by 1.5-inch steel. The area covering 3 by 3 voxels (indicated by the boxes in these images) was used to analyze the image quality. Images (d), (e), and (f) are the processed radiography images using a Fourier filter, which enhances the uranium disk image by suppressing the image of the grids of the CsI detector. This demonstrated that a more uniform radiography image can be obtained with post-processing to help distinguish the target.

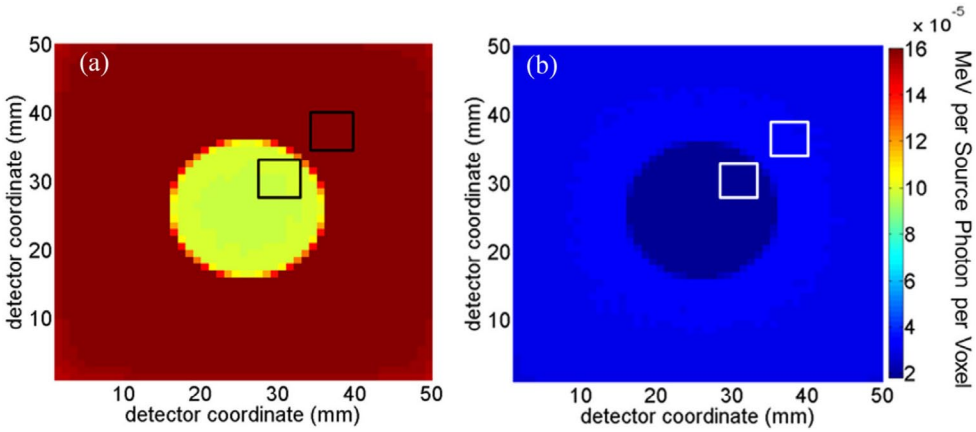

Fig. 5. MCNPX simulation of the shielded uranium radiography. The image contrast is calculated with 9 voxels (indicated by the boxed areas). (a) The simulated radiograph of 6-mm shielded uranium, shows an image contrast of 0.40. (b) The simulated radiograph of 8-mm shielded uranium, has an image contrast of 0.42.

trast and dose depend on X-ray energy spread. In this section, we use MCNPX simulations to address these questions and systematically study the advantages of narrowband X-ray beams for cargo container radiography. This includes a comparison of narrowband X-ray beams to bremsstrahlung sources for radiography of shielded uranium in terms of dosage. The comparison shows that X-ray bandwidth up to 40% does not affect the image contrast, and the narrowband X-ray source reduces on-target dose by 2 times and bystander dose by 10 times compared with a bremsstrahlung source with the same end point energy.

3.1. Effect of X-ray bandwidth on radiography image

To confirm the previously stated conclusion that up to 40% bandwidth of the X-ray beam at 6 MeV has little effect on radiography, we studied the image contrast of a narrowband X-ray source with different energy spreads. The simulation geometry is shown in Fig. 6. A 6-mm glass window in between the X-ray source and wood pallet is taken into account because the window is needed to keep the X-ray source in vacuum. The wood pallet has dimensions of 107 cm by 107 cm by 101 cm; a 5-cm length HEU cube is located in the center. A 1.5-cm thick $CdWO_4$ detector is used in the simulation since it is a common detector for cargo container radiography. We also added the space between the X-ray source, pallet, and detector to account for the effect of air in this space.

Fig. 7 shows the mid-plane lineout of deposited energy per photon source with X-ray beams with different central energies and bandwidth. By comparing these two cases, we found that the image contrast of a radiography taken with 40% energy spread is nearly the same as one taken with an X-ray beam with 10% energy spread. X-ray beams with 40% energy spread have about 1% greater transmission ratio. This showed that the currently achieved energy spread of the Compton X-ray source is sufficient to provide the advantages of monoenergetic X-ray radiography.

This simulation also provides a way to determine the X-ray flux that is required for radiography. Though the required X-ray source flux for cargo container scanning depends on various parameters, such as materials inside the cargo container, scan speed, detector sensitivity, and scan distance, the wood pallet is representative of typical cargo composition. We adopted the criteria that photon energy equal to 10 MeV needs to be deposited on a 1 cm^2 detector to form a radiography image [22]. With this criterion, we found that 10^5 photon/cm^2 is required to form a radiographic image with a narrow bandwidth X-ray source for the wood pallet, since the energy deposited on the detector is a factor of 10^{-4} of the source photon energy. Assuming a cargo container with a height of 2 m, and a required scan speed of 10–100 cm s^{-1}, a photon flux of 10^8–10^9 photons per second is needed for the radiography. The maximum scan rate will be limited by the level of attenuation the X-ray beam experiences due to objects in the cargo container.

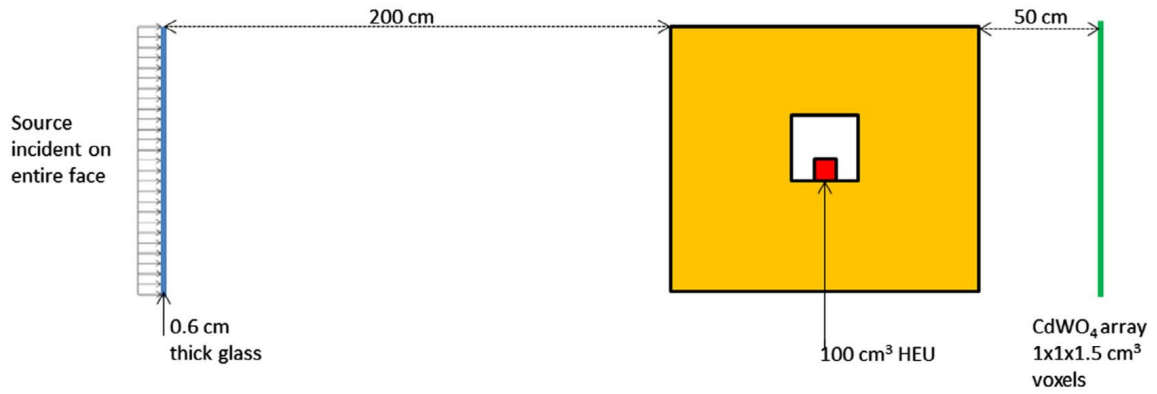

Fig. 6. Simulation setup for the wood pallet illuminated with an X-ray beam that is transmitted through a glass window, propagated 2 m in air, and is then detected using a $CdWO_4$ array located 0.5 m after pallet.

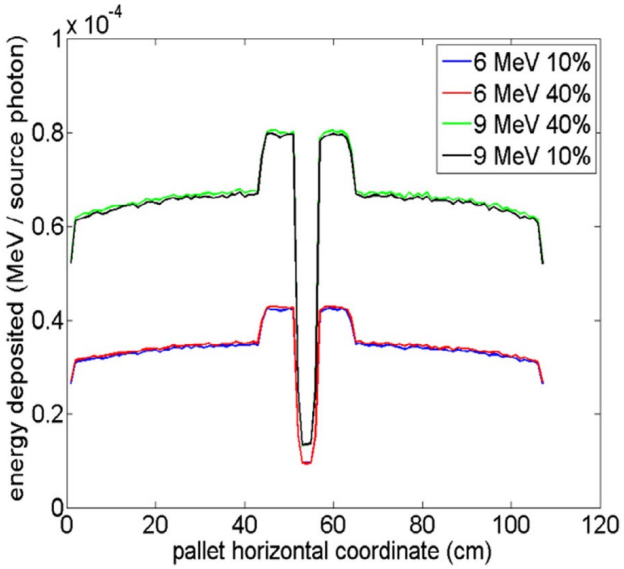

Fig. 7. Mid-plane cross sections of the energy deposited on the detector after transmission through the wood pallet per source photon for 6 and 9 MeV X-rays with 10% and 40% bandwidth.

3.2. On target dose reduction

Another interesting question for narrow bandwidth radiography is the on-target dose compared with a bremsstrahlung source. A bremsstrahlung source has a larger portion of lower energy photons (<1 MeV), which results in a much larger fraction of absorption and scattering by the target. This leads to higher dose deposition on target. Using the same pallet setup as shown in Fig. 6, we quantitatively evaluated the dose deposited on the target of different X-ray sources. To obtain and compare the absolute dose, we used the energy deposited on the detector as the criteria. In another words, the on-target doses are compared with the same image intensity obtained on the detector for different X-ray sources.

The results shown in Fig. 8 indicate that a narrowband source at 6 MeV with 40% energy spread deposited two times less dose on target than a bremsstrahlung source with the same end point energy. In addition, we compared the deposited dose on the target between a 9-MeV narrowband X-ray source and the bremsstrahlung source with 9-MeV endpoint energy, and this also showed a dose reduction by a factor of two for the narrowband X-ray source. Using the same criteria, we studied the bystander dose at 1 m away from the edge of the pallet. In this case, we found that the narrowband X-ray beam reduced the bystander dose by a factor of 10 as compared with the bremsstrahlung source at the same end-point energy. This X-ray source therefore provides a better fit to the ALARA requirement for cargo interrogation [21].

3.3. Standoff propagation

The highly collimated inverse-Compton X-ray beam is also advantageous for standoff interrogation. If we assume that a bremsstrahlung source has a photon number of 10^{14}/s (which is typical for those used for cargo container screening) distributed in a 60 degree half cone angle, the corresponding photon flux is 3.2×10^{13}/s/sr. For LWFA-ICS with 10 Hz repetition rate, 4 mrad divergence angle, and 10^7 photon/shot, the photon flux is 8×10^{12}/s/sr. Taking into account the narrow bandwidth, the LWFA-ICS should have comparable or even higher photon flux/ bandwidth in the MeV range compared with the bremsstrahlung source. By increasing the current inverse Compton source repetition rate, such as using a 50-Hz diode pumped laser system, and increasing electron beam charge to the nC level, the X-ray flux from LWFA-ICS sources can be further increased by more than one order of magnitude [23–25].

We simulated the long-standoff propagation of an X-ray beam with central energy of 9 MeV, energy spread of 10% FWHM, and 1×10^7 photons per pulse at 10 Hz. The divergence of the photon beam is analyzed by simulating its propagation over a 100-m long cylindrical column of air, with a 3-m radius. The beam is simulated as a cone with an opening angle of 2 mrad, which corresponds to the measured X-ray half cone angle at 9 MeV. Fig. 9 shows the spread of the beam at 100 m from the source. The results show that the beam is still concentrated in a 20-cm radius from the center of the beam. The X-ray attenuation due to air at this distance is 18.5%. Fig. 10 shows the evolution of the X-ray beam spectrum as a function of distance at 0 m, 50 m and 100 m. The X-ray spectrum shape has no significant change except at the low energy end (<1 MeV), which is due to the inelastic scattering and the excitations of the atoms and molecules in air.

The bystander dose is also of interest at different points along the beam line for the standoff scenario. Fig. 11 shows doses measured at 10-m increments along the beam simulated by the MCNPX code.

From the simulation results, the attenuation of the X-ray beam is 18.5% for 100-m propagation without significant change on the spectrum shape, and the bystander dose is much less than the NRC limit of 5 mrem/h. These results demonstrate that the inverse-Compton source with narrow beam divergence is suitable for standoff interrogation.

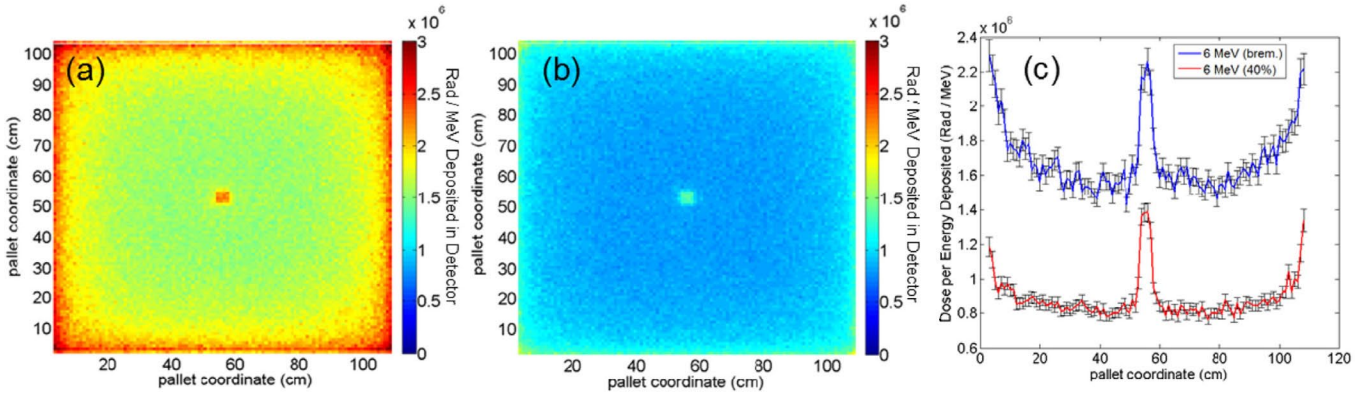

Fig. 8. MCNPX simulation of the on-target dose comparison of a 6-MeV narrowband X-ray source and bremsstrahlung source. (a) Dose map of 6 MeV narrowband source with rad per MeV photon energy deposited on the detector. (b) Dose map of 6 MeV bremsstrahlung source with rad per MeV photon energy deposited on the detector. (c) Midplane cross sections of the dose map for two different 6 MeV sources. The error bars represent the standard deviation of the numerical simulation.

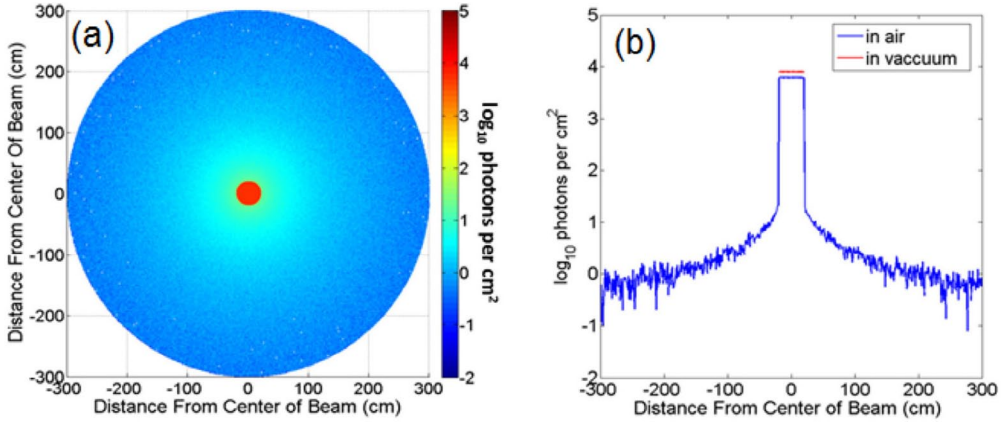

Fig. 9. MCNPX simulation of 100 m X-ray propagation in air. (a) Photon flux map 100 m from source, per pulse. The red circle shows the X-ray beam size if it propagates in vacuum without scattering. (b) Lineout of the photon distribution along the photon flux map center. The red line showed flux of photon if the X-ray beam propagates in vacuum without attenuation.

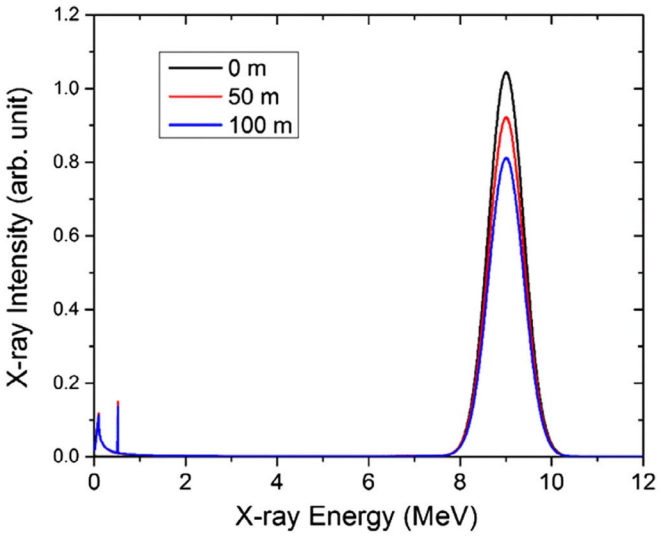

Fig. 10. Spectral evolution of a 9 MeV X-ray beam with 10% energy spread as it propagates in air. The black line shows the original X-ray spectrum. The red and blue lines show the X-ray spectrum after 50 m and 100 m propagation, respectively.

4. Summary

Using both experiments and simulations, we studied the performances of various X-ray sources for shielded cargo radiography. The MCNPX simulations showed that a narrowband X-ray source with energy spread of ~40% results in significant dose reduction. Such narrow bandwidth has already been demonstrated experimentally by an LWFA-ICS X-ray source at the University of Nebraska-Lincoln [26]. We also experimentally demonstrated the capability of this LWFA-ICS source to obtain a single-shot radiograph of an 8-mm thick uranium disk, shielded with 76-mm steel, with an image contrast of 0.4 and SNR of 2. In terms of the on-target dose, the simulation study showed that narrowband X-ray beams are superior to bremsstrahlung X-rays with the same endpoint energy. When comparable radiographic image quality is used as the comparison criteria, we find that the dose is not reduced by the large amount expected from previous studies [9,26]. The reason is that there is a relatively flat X-ray attenuation curve in the MeV range, and therefore a large portion of X-ray photons from the 6 to 9 MeV bremsstrahlung source contributes to the radiographic image. We also found that other features of LWFA-ICS X-rays, such as the small divergence, makes the source suitable for both standoff interrogation and scanning in pencil-beam mode. In addition, the narrow bandwidth and high energy of the LWFAICS X-ray source permits improvement of material discrimination through dual energy radiography [27–30], as well as implementation of sensitive threat alarms for

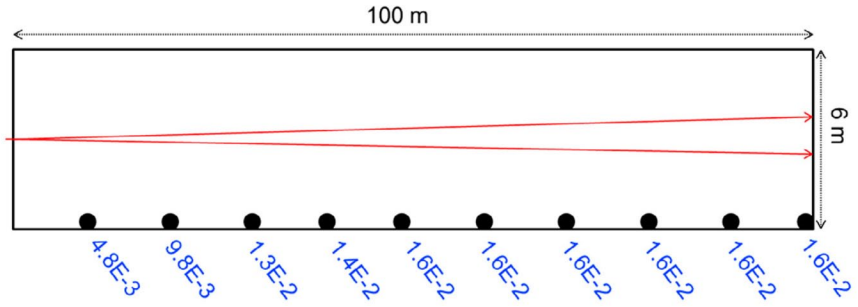

Fig. 11. Dose rates (mrem/h) at a distance of 3-m off-axis from the 9-MeV X-ray beam in a 2-mrad cone with 108 photons/s.

isotope specific detection. The X-ray system reported here occupies ~400 ft^2 (inclusive of both the laser system and the inverse-Compton source), and can fit on a flatbed truck for applications. Given these many advantages, LWFA-ICS X-ray sources are potentially transformative for shielded radiography.

Acknowledgments — We thank K. Brown, J. Mills, and C. Petersen for their contributions to the laser facility, and thank N. Glasco for proofreading the manuscript. This material is based on work supported by the US Department of Energy (DOE), Office of Science, Basic Energy Sciences (BES), under Award #DE-FG02-05ER15663 (ultrafast X-ray science); the Air Force Office for Scientific Research, FA9550- 11-1-0157 (high-field laser-electron scattering); the Department of Homeland Security Domestic Nuclear Detection Office, under competitively awarded contract HSHQDC-13-C-B0036 (low-dose X-ray radiography); and National Strategic Research Institute, FA4600-12-D-9000 (selective photo-activation analysis). This support does not constitute an express or implied endorsement on the part of the Government.

References

[1] G. Allison, Nuclear Terrorism Fact Sheet, Belfer Center for Science and International Affairs, Harvard Kennedy School, April 2010. Belfer Center for Science and International Affairs.
[2] Container Security Initiative in Summary, U.S. Customs and Border Protection, U.S. Department of Homeland Security, May 2011.
[3] Jonathan Medalia, Detection of Nuclear Weapons and Materials: Science, Technologies, Observations, CRS Report for Congress, 2010, pp. R40154.
[4] G.M. Gaukler, C. Li, R. Cannaday, S.S. Chirayath, Y. Ding, Detecting nuclear materials smuggling: using radiography to improve container inspection policies, Ann. Oper. Res. 187 (2011) 65–87.
[5] D. Slaughter, M. Accatino, A. Bernstein, J. Candy, A. Dougan, J. Hall, A. Loshak, D. Manatt, A. Meyer, B. Pohl, Detection of Special Nuclear Material in Cargo Containers using Neutron Interrogation, Lawrence Livermore National Laboratory, 2003.
[6] P. Baesso, D. Cussans, C. Thomay, J. Velthuis, Toward a RPC-based muon tomography system for cargo containers, J. Instr. 9 (2014) C10041.
[7] G. Chen, Understanding X-ray cargo imaging, Nucl. Instr. Meth. Phys. Res. Sect. B 241 (2005) 810–815.
[8] P. Bjorkholm, Cargo Screening: Selection of Modality, 17, Port Technology International, 2003, pp. 37–39.
[9] Victor Orphan, Ernie Muenchau, Jerry Gormley, Rex Richardson, Advanced Cargo Container Scanning Technology Development, Science Applications International Corporation, San Diego, California.
[10] D.R. Norman, J.L. Jones, B.W. Blackburn, A. Fisher, S.M. Watson, K.J. Haskell, A. W. Hunt, M. Balzer, Radiation safety aspects for pulsed photonuclear assessment techniques in outdoor operations, Nucl. Instr. Meth. Phys. Res. Sect. B 261 (2007) 913–917.
[11] R. Bentley, Database of high-Z signatures in Cargo, technologies for homeland security (HST), in: 2011 IEEE International Conference on, 2011.
[12] A. Zavadtsev, D. Zavadtsev, A. Krasnov, N. Sobenin, S. Kutsaev, D. Churanov, M. Urbant, A dual-energy linac cargo inspection system, Instr. Exp. Tech. 54 (2011) 241–248.
[13] B.R. Grogan, J.J. Henkel, J.O. Johnson, J.T. Mihalczo, T.M. Miller, B.W. Patton, Investigation of active interrogation techniques to detect special nuclear material in maritime environments: boarded search of a cargo container ship, Nucl. Instr. Meth. Phys. Res. Sect. B 316 (2013) 62–70.
[14] H.R. Weller, M.W. Ahmed, H. Gao, W. Tornow, Y.K. Wu, M. Gai, R. Miskimen, Research opportunities at the upgraded HI gamma S facility RID G-2589-2011, Prog. Part. Nucl. Phys. 62 (1) (2009) 257–303.
[15] F. Albert, S.G. Anderson, D.J. Gibson, C.A. Hagmann, M.S. Johnson, M. Messerly, V. Semenov, M.Y. Shverdin, B. Rusnak, A.M. Tremaine, F.V. Hartemann, C.W. Siders, D.P. McNabb, C.P.J. Barty, Characterization and applications of a tunable, laser-based, MeV-class compton-scattering gamma-ray source, Phys. Rev. Spec. Top. Accel. Beams 13 (2010) 070704.
[16] S. Chen, N.D. Powers, I. Ghebregziabher, C.M. Maharjan, C. Liu, G. Golovin, S. Banerjee, J. Zhang, N. Cunningham, A. Moorti, S. Clarke, S. Pozzi, D.P. Umstadter, MeV-energy X-rays from inverse compton scattering with laser-wakefield accelerated electrons, Phys. Rev. Lett. 110 (2013) 155003.
[17] N.D. Powers, I. Ghebregziabher, G. Golovin, C. Liu, S. Chen, S. Banerjee, J. Zhang, D.P. Umstadter, Quasi-monoenergetic and tunable X-rays from a laser-driven compton light source, Nat. Photonics 8 (2014) 29–32.
[18] C. Liu, G. Golovin, S. Chen, J. Zhang, B. Zhao, D. Haden, S. Banerjee, J. Silano, H. Karwowski, D. Umstadter, Generation of 9 MeV c-rays by all-laser-driven compton scattering with second-harmonic laser light, Opt. Lett. 39 (2014) 4132–4135.
[19] S. Banerjee, S. Chen, N. Powers, D. Haden, C. Liu, G. Golovin, J. Zhang, B. Zhao, S. D. Clarke, S. Pozzi, J. Silano, H.J. Karwowski, D. Umstadter, Compact source of narrowband and tunable X-rays for radiography, Nucl. Instr. Meth. Phys. Res. Sect. B 350 (2015) 106–111.
[20] M.A. Flower, Webb's Physics of Medical Imaging, CRC Press, 2012.
[21] CFR 20.1003, US Nuclear Regulatory Commission, 2009.
[22] J.I. Katz, G.S. Blanpied, K.N. Borozdin, C. Morris, X-radiography of cargo containers, Sci. Global Secur. 15 (2007) 49–56.
[23] J. Tümmler, R. Jung, H. Stiel, P. Nickles, W. Sandner, High-repetition-rate chirped-pulse-amplification thin-disk laser system with joule-level pulse energy, Opt. Lett. 34 (2009) 1378–1380.
[24] C. McGuffey, A.G.R. Thomas, W. Schumaker, T. Matsuoka, V. Chvykov, F.J. Dollar, G. Kalintchenko, V. Yanovsky, A. Maksimchuk, K. Krushelnick, V.Y. Bychenkov, I.V. Glazyrin, A.V. Karpeev, Ionization induced trapping in a laser wakefield accelerator, Phys. Rev. Lett. 104 (2010) 025004.
[25] A. Pak, K.A. Marsh, S.F. Martins, W. Lu, W.B. Mori, C. Joshi, Injection and trapping of tunnel-ionized electrons into laser-produced wakes, Phys. Rev. Lett. 104 (2010) 025003.
[26] S.M. Khan, P.E. Nicholas, M.S. Terpilak, Radiation dose equivalent to stowaways in vehicles, Health Phys. 86 (2004) 483–492.
[27] S. Ogorodnikov, V. Petrunin, Processing of interlaced images in 4–10 MeV dual energy customs system for material recognition, Phys. Rev. Spec. Top. Accel. Beams 5 (2002) 104701.
[28] M. Gmar, E. Berthoumieux, S. Boyer, F. Carrel, D. Doré, M. Giacri, F. Lainé, B. Poumarède, D. Ridikas, A. Van Lauwe, Detection of nuclear material by photon activation inside cargo containers, Defense and Security Symposium, 2006.
[29] H. Im, K. Song, Applications of prompt gamma ray neutron activation analysis: detection of illicit materials, Appl. Spectrosc. Rev. 44 (2009) 317–334.
[30] G. Zentai, X-ray imaging for homeland security, Int. J. Signal Imag. Syst. Eng. 3 (2010) 13–20.